






Atomically resolved study of the unpinned GaN (10 $\bar{1}$ 0) surface by cross-sectional scanning tunneling microscopy

E. G. Banfi ^{1,*}, T. J. F. Verstijnen ¹, E. Monroy ², M. E. Flatté ^{3,1} and P. M. Koenraad ¹

¹*Department of Applied Physics and Science Education, Eindhoven University of Technology, Eindhoven 5612 AZ, The Netherlands*

²*Université Grenoble-Alpes, CEA, Grenoble INP, IRIG, PHELIQS, 17 avenue des Martyrs, 38000 Grenoble, France*

³*Department of Physics and Astronomy, University of Iowa, Iowa City, Iowa 52242, USA*



(Received 22 March 2023; accepted 18 July 2023; published 15 August 2023)

Gallium nitride has been studied thoroughly in recent decades as the material is relevant for applications in blue-light-emitting devices and laser diodes, as well as high-power and high-frequency transistors. This material has rarely been explored by cross-sectional scanning tunneling microscopy (X-STM), in spite of the relevance of its m plane, which constitutes the output facet of commercial lasers and the sidewalls of GaN nanowires, and has been intensively explored as an alternative orientation for light emitters due to its nonpolar nature. Here we successfully investigate a clean m plane of wurtzite GaN and study the presence of gallium vacancies by X-STM at liquid nitrogen temperature. We observe Friedel oscillations around the defects and characterize the dependence of the oscillation radius on the applied bias. This physical phenomenon, combined with the tunneling conditions, clarifies the charge state of the vacancy and the origin of the free carriers in GaN that screen the Ga vacancies. We observe a predicted bi-stability of the N atom neighboring the Ga vacancy and perform density functional theory calculations to complement the experimental results. We obtain high-quality clean cleavages on the GaN m plane, which will allow for the study of other nanostructured GaN-based materials and devices.

DOI: [10.1103/PhysRevB.108.085304](https://doi.org/10.1103/PhysRevB.108.085304)

I. INTRODUCTION

Wide-band-gap semiconductors (WBSs) fulfill the requirements of applications in high-power and high-frequency electronics. Gallium nitride is a WBS with a direct Γ -point band gap of 3.4 eV that has been extensively studied in the last three decades. This material is used for blue-light-emitting devices [1], UV laser diodes [2], high-electron mobility [3], ferroelectric field-effect transistors [4], and other devices [5–9]. Despite this, research on atomically resolved GaN surfaces to study these structures with scanning tunneling microscopy (STM) is limited [10–13]. Bulk GaN has been extensively studied using density functional theory (DFT) in terms of defects [14,15] and electronic properties [15–17]. While some work has been performed on defects of m -plane GaN with DFT [18], the combination of STM and DFT to improve our understanding of this surface is still underutilized.

The most stable GaN crystalline structure is wurtzite, and it has a tendency to grow along the $\langle 0001 \rangle$ c axis. However, the presence of polarization along this axis has motivated a plethora of studies on alternative crystallographic orientations [19], including not only the nonpolar a - $(11\bar{2}0)$ and m - $(10\bar{1}0)$ planes but also semipolar planes like $(11\bar{2}2)$ and $(2\bar{2}01)$. Among them, the m plane is one of the most studied orientations due to its reduced anisotropy, which allows planar growth in conditions similar to those of c -GaN [20]. LEDs

were rapidly demonstrated on this plane that hold the record modulation bandwidth in nitride LEDs [21]. It is also the preferred plane for research on far-infrared intersubband devices due to the simplicity of their design and doping [22–24]. Fundamental studies of the m plane have gained relevance with the boom in nanowire technology since the natural sidewalls of self-assembled GaN nanowires and nanowires resulting from selective area growth are m oriented [25,26]. The m plane is the natural facet of GaN lasers since it is the plane easiest to cleave [27] and it can be exposed by KOH-based crystallographic-selective etching [28].

STM provides a unique perspective in surface characterization, providing access to topography and also electronic effects in the probed surface. In particular, cross-sectional STM (X-STM) allows the study and characterization of semiconductor heterostructures such as quantum wells and quantum dots, providing detailed information on size, shape, compositional uniformity, interface roughness, etc. [29–32]. In doped semiconductors, X-STM can provide information about the distribution, clustering, and electronic features of the doping atoms [33–36]. Yet as powerful as it is, X-STM has some constraints; the sample must show good conductivity, and the requirement for a natural cleaving plane to obtain atomically flat surfaces limits its application.

In this work we present a detailed, atomically resolved X-STM study of GaN m planes $\{1\bar{1}00\}$ as well as DFT calculations of defects in this surface. GaN presents several challenges for X-STM imaging, as it has a wide band gap, which leads to conductivity issues, and the wurtzite lattice presents two classes of nonpolar planes along which the

*e.g.banfi@tue.nl

natural cleaving could propagate, resulting in rough cleaved surfaces.

II. METHODS

The sample we studied is a commercial freestanding GaN wafer from Nanowin. The specific resistivity at room temperature is $<0.5 \Omega \text{ cm}$, and the dislocation density is $<5 \times 10^6 \text{ cm}^{-2}$. The sample is not intentionally doped, but GaN tends to be naturally *n* type [37–40]. All the X-STM measurements were carried out in a commercial Scienta Omicron low-temperature STM at liquid nitrogen temperature (LNT). The setup is in ultrahigh vacuum (UHV) with a pressure of $4\text{--}6 \times 10^{-11} \text{ mbar}$. The samples were cut from the wafer with a parallelogram shape, with the long sides following the *m* planes $\{1\bar{1}00\}$ (dimensions of $4 \times 8 \text{ mm}^2$). The prepared samples were loaded in the system and baked at 180°C to remove contaminants and then cooled down to LNT, followed by cleaving in UHV right before measurement. The cleave exposed a fresh new *m* plane that was measured. The combination of LNT and UHV allows the sample surface to remain clean with few to no contaminants for a prolonged time (days).

The STM tips were fabricated starting from a polycrystalline W wire followed by electrochemical etching in a 2 M solution of KOH. The prepared tips were then loaded in the system, where they were baked at 230°C , followed by Ar sputtering to remove the W oxide scale that forms on the tip surface during the etching.

In an STM measurement, both electronic and topographic effects contribute to the image. In this work, all the reported images were taken in constant-current mode.

The calculations performed in this study are made in the DFT framework using projector augmented wave pseudopotentials [41] in the Vienna Ab initio Simulation Package (VASP) code [42,43]. The exchange-correlation interaction between electrons is described using the Perdew-Burke-Ernzerhof (PBE) form of the generalized gradient approximation (GGA) [44].

The GaN supercell considered in this work consists of a 5×4 surface supercell that is five monolayers thick and has 12 \AA of vacuum between slabs. Of these five monolayers the bottom two are fixed in their bulk configuration to simulate bulk behavior under the slab surface. The cell consists of 200 Ga and 200 N atoms. The sampling of the Brillouin zone is done using a $4 \times 4 \times 1$ Monkhorst-Pack grid. The energy cutoff used to describe the plane waves is 400 eV. The lattice constants found for this cell are $a = 3.23 \text{ \AA}$ and $c = 5.28 \text{ \AA}$, while the experimental values are $a = 3.19 \text{ \AA}$ and $c = 5.19 \text{ \AA}$ [45]. These values are reasonable since GGA-PBE is known to overestimate lattice constants slightly.

III. RESULTS AND DISCUSSION

A. General appearance

In Fig. 1(a), we show a $28 \times 28 \text{ nm}^2$ negative bias image of a clean wurtzite GaN $\{1\bar{1}00\}$ surface. Obtaining a clean surface without a high density of defects has been shown to be challenging [10–13,46]. We managed to obtain such a

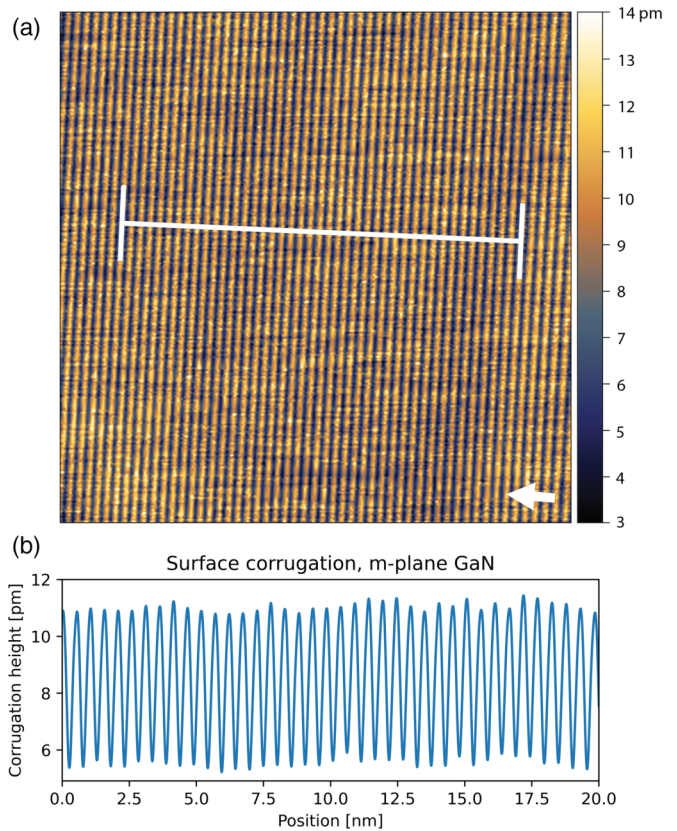


FIG. 1. (a) A $28 \times 28 \text{ nm}^2$ X-STM topographic image of the clean GaN $\{1\bar{1}00\}$ surface measured at -1.8 V and 50 pA tunneling conditions. The color scale on the side shows the height variation in the image in picometers. The white arrow indicates the growth direction $[0001]$, and the white line indicates where the line profile in (b) was taken.

surface by cleaving in UHV ($4\text{--}6 \times 10^{-11} \text{ mbar}$) a freestanding GaN wafer thinned down to a thickness of about $150 \mu\text{m}$. Per experiment, we prepared three samples, and on average, only one was cleaved with a flat enough surface for our STM analysis. The main problem is related to the natural cleaving planes of wurtzite GaN, which allow the samples to cleave in different directions along the *m* planes or the *a* planes. Therefore, the cleaving can lead to a staggered surface, or the sample cleaves along a direction nonorthogonal to our STM tip. An accurate small incision to direct the cleaving and clamping the sample perfectly parallel to the natural cleaving plane substantially increase the likelihood of a successful cleavage. In our experiments we observed very clean surfaces with no contamination even several days after the cleaving.

In Fig. 1(a), we show a negative bias image of a clean wurtzite GaN $\{1\bar{1}00\}$ surface. In contrast to GaAs and, due to the wide-band-gap characteristic of GaN, under a negative bias, we still observe the empty states instead of the filled states. This happens due to tip-induced band bending (TIBB) [47]. When applying a negative bias, TIBB bends the conduction band (CB) downwards, eventually crossing the Fermi energy and creating an accumulation region on the surface of the material, as schematically shown in Fig. 2. This accumulation region becomes a source for tunneling electrons, as

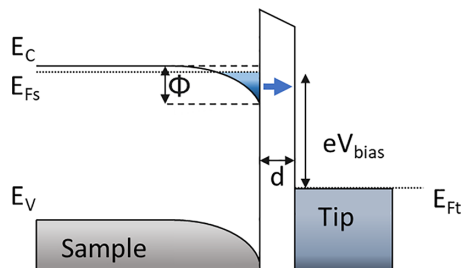


FIG. 2. Simplified model of the band bending occurring due to TIBB in the case of an n -type wide-band-gap semiconductor. E_C , E_V , E_{F_S} , and E_{F_T} are, respectively, the sample conduction band minima, sample valence band maxima, sample Fermi energy, and tip Fermi energy. eV_{bias} is the energy related to the tip-sample applied bias, d is the tip-sample distance, and Φ represents the band bending of the conduction band. The blue-shaded area in the sample surface represents the accumulation region. The blue arrow represents the tunneling current arising from the accumulation region electrons.

previously predicted [48–50] and as schematically shown in Fig. 2 by the blue arrow and in the $I(V)$ curve measured on this sample in Fig. 3. As we can see from the $I(V)$ curve, in the negative bias region around -2 V the current increases above the experimental noise level, and around -3 V we observe a change in the slope. The simulated $I(V)$ curves prove that the current arising at -2 V is only due to CB accumulation layer

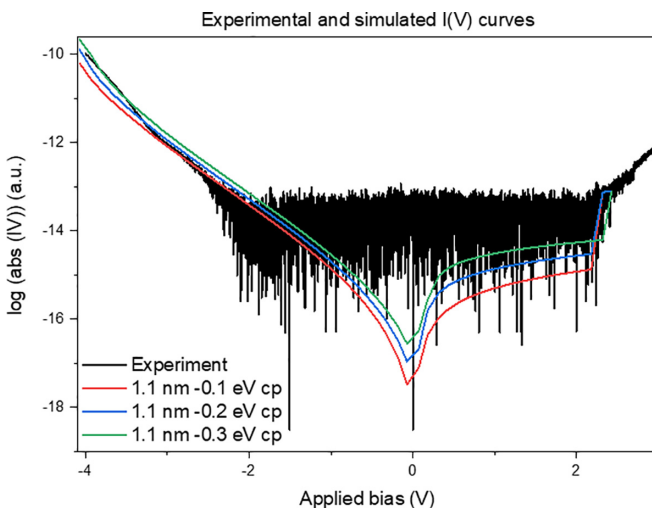


FIG. 3. Experimental and simulated $I(V)$ curves. The black line is measured on the clean m plane of GaN (250 pA and 5 V set points). Approaching from the positive side, the curve falls to the noise floor level (10^{-13}) of the $I(V)$ converter at 2 V until -2 V, where it starts to pick up again. When further lowering the bias, we see a second contribution at -3 V as a change in the slope of the curve. The simulated curves (red, blue, and green) were obtained using the SEMITIP software developed by Feenstra [47,51,52]. The tip-sample distance was set at 1.1 nm. The contact potential (cp) is a parameter related to the offset between the Fermi levels of the sample and the tip. Since W tips can have different Fermi energy level positions depending on the atomic configuration on the apex of the tip, we varied the cp until it gave us a good resemblance to the experiment. The simulations above 2 V did not converge to a finite current value.

electrons. At a higher bias (-3 V) when there is a change in the slope, the valence band (VB) starts to contribute.

The height profile shown in Fig. 1(b) shows a surprisingly small corrugation amplitude (peak to valley height difference) of 5 pm. On a standard $\{110\}$ GaAs surface we reproducibly obtain a 20 to 50 pm corrugation height, while on GaN $\{1\bar{1}00\}$ the corrugation amplitude is 4 to 10 times smaller in comparison. This is a rather characteristic feature of the material that presented itself in every measurement.

B. Friedel oscillations

While measuring the m -plane surface of GaN, we observed features such as those displayed in Figs. 4(a) and 4(b). These features consist of a very dark deep core surrounded by a halo of enhanced contrast, as shown in the STM height profiles in Figs. 4(c) and 4(d). The features have a circular symmetry hinting at a pointlike source. Similar features related to Friedel oscillations were already observed around single Si dopants in GaAs [53–55]. In order to create a Friedel oscillation in a semiconductor it is necessary to have a charged impurity or defect and free carriers. The impurity introduces an electric field that perturbs its surroundings, wherein the free carriers react to this electric field by screening it.

When a negative bias is applied, TIBB bends the conduction band downwards, eventually crossing the Fermi energy and creating an accumulation region on the surface of the material, as schematically shown in Fig. 2. When the bias is further lowered to establish tunneling from the valence band, the accumulation region tunneling current becomes orders of magnitude greater than the one arising from the valence band. This process of surface accumulation may happen in any STM measurement on a semiconductor when the right conditions are met [47].

In our experiment, the observed features are negatively charged, as we can deduce from the contrast difference with their surroundings. Dark contrast in STM has two possible origins: either the region is physically lower, or the surface local density of states (LDOS) that contributes to the tunneling current is smaller. The former case was excluded since the feature sizes varied with the applied bias. Since the images reported in this work were taken at negative bias and the free carriers are CB accumulation layer electrons, the latter case requires a negative charge. The negative charge will locally shift the bands upwards, a reduction in Φ in Fig. 2. This will reduce the effective LDOS available for tunneling and will subsequently force our tip to get closer to the surface to keep the current set point.

Thus, all the requirements to create the Friedel oscillation are met. In fact, we observed, as shown in Figs. 4(c), 4(d), and 5, that the size and intensity of the oscillation change when the applied bias between the tip and sample is varied. In Fig. 4(c) we report the line profile measured at -1.8 V (red line) and at -3.0 V (black line). If we compare the oscillation depth and diameter to the corrugation that is visible in both profiles in Fig. 4(c), we can see that the red profile is both wider (around 15 versus 8 nm) and deeper (up to 120 versus 90 pm) than the black profile. This can be understood by considering that the larger bias produces a stronger TIBB, bending the conduction band further below the surface Fermi energy and

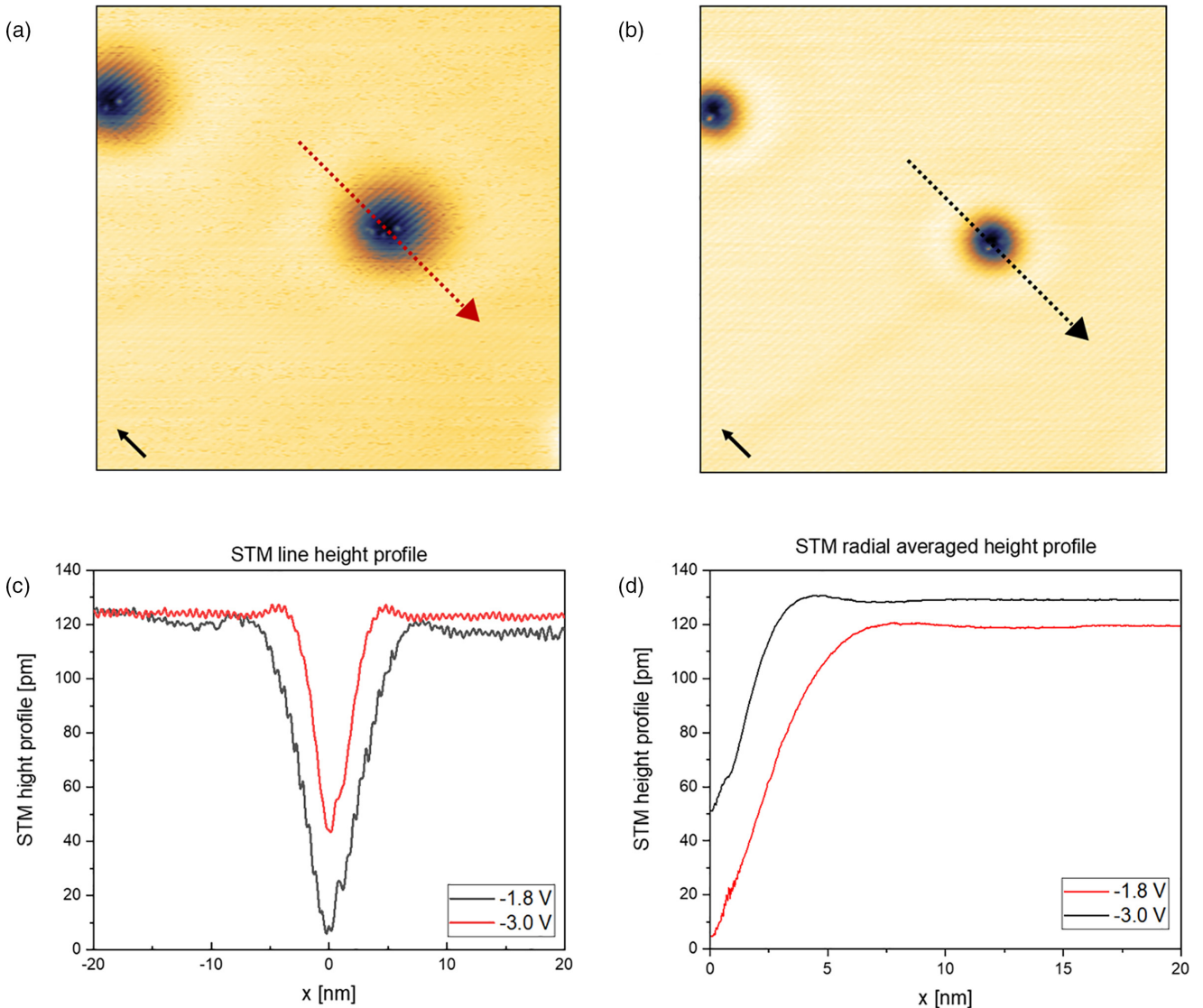


FIG. 4. (a) and (b) $40 \times 40 \text{ nm}^2$ X-STM images of the GaN *m* plane taken at -1.8 and -3.0 V, respectively, and 50 pA . The solid arrow in the bottom left corner indicates the growth direction $[0001]$. The dotted arrow indicates the location and the direction of the line height profile reported in (c). In (d) we report the same profiles shown in (c), but radially averaged, highlighting the presence of the charge ring around the feature.

creating a stronger accumulation region with more electrons. This stronger accumulation creates a denser two-dimensional electron gas that is more efficient at screening the charged feature, and therefore, the oscillation is both shallower and narrower.

We performed a series of voltage-dependent measurements on the feature shown in Figs. 4(a) and 4(b). In Figs. 5(a) and 5(b) the relation between the Friedel oscillation around the charged defects and the applied bias is shown. Figure 5(a) shows the radial average of the linear profiles at seven different biases obtained for the same feature. In order to clearly show the contrast profile around these defects we make azimuthal averaged radial profiles; that is, the profiles starting at the defect site are averaged over 360° around these defects. The bias is swept from -2.5 to -1.9 V. From these seven curves we see how the radius of the oscillation increases, starting from a value of $5.5 \pm 0.5 \text{ nm}$

at -2.5 V to $8.5 \pm 0.5 \text{ nm}$ at -1.9 V. In Fig. 5(b) we report the position of the local maximum per curve reported in Fig. 5(a) that corresponds to the Friedel oscillation radius. In Fig. 5(b) we observe a decrease in the oscillation radius with the increase in the strength of the applied bias. The relationship of the oscillation radius to the applied bias thus proves an electron accumulation region induced by TIBB.

It is relevant to point out that, as already mentioned in Sec. III A, the corrugation height in this sample is smaller than the typical corrugation observed in GaAs. If we consider, for instance, the case of Si-doped GaAs [53], the feature height is about 120 pm , and the ratio of atomic corrugation and feature contrast is about 2 to 4. This allows us to easily spot the feature and see the corrugation at the same time. Meanwhile, on the *m* plane of GaN the corrugation height is around 5 pm , and the ratio of atomic corrugation and feature contrast ($90\text{--}120\text{pm}$) is therefore around 20 (depending on the applied bias),

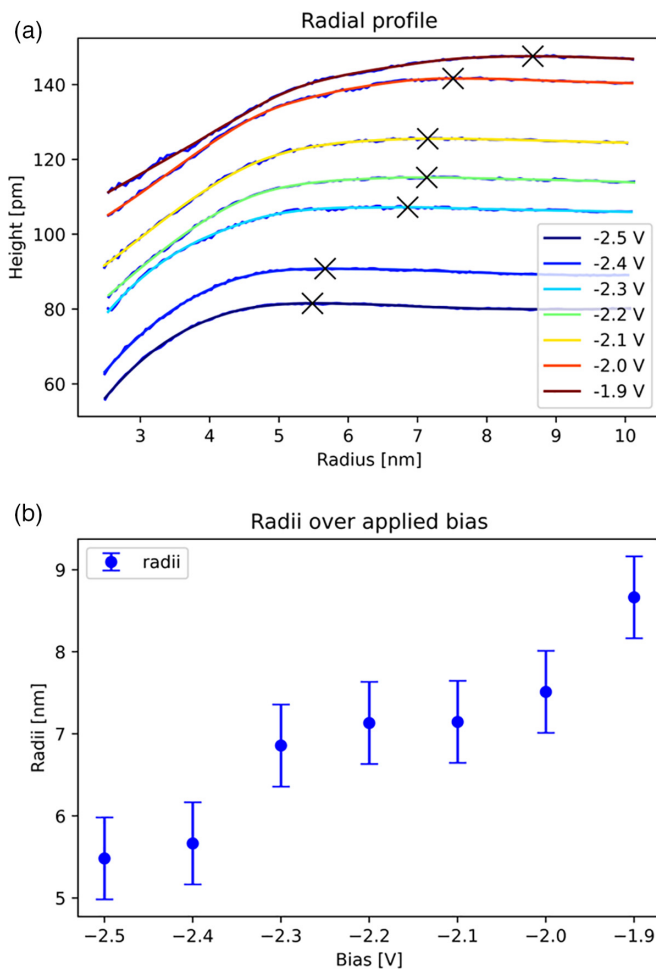


FIG. 5. (a) shows the radial average of the linear profiles taken for one feature at seven different biases. Each line is vertically shifted by 10 pm to increase visibility. The bias goes from -2.5 to -1.9 V, while all the other tunneling parameters are kept constant during the voltage swipe. The current set point is 50 pA. The raw profile and a filtered version are superimposed. The curves were filtered with the Savitzky-Golay filter of the PYTHON library SCIPY.SIGNAL, version 1.9. The central region between 0 and 2.5 nm of the curves is rather noisy and is removed. In (a) the cross indicates the position of the local height maximum of each profile. The positions of these maxima correspond to the radius of the Friedel oscillations, and these points are plotted in (b) versus bias.

producing a more dramatic contrast where, while it is still present, the corrugation is less apparent, hidden in the bright part of the color scale.

C. Free versus pinned surface

In Fig. 1(a), we show a negative bias image of a clean wurtzite GaN $\{1\bar{1}00\}$ surface. When imaging the $\{110\}$ zincblende surface on materials such as GaAs using X-STM, it is possible to selectively image filled or empty states by applying a negative or positive bias, respectively, between the tip and sample [56]. This is due to the nature of the $\{110\}$ surface. During cleaving, the atoms and dangling bonds on the surface are rearranged to compensate the charge transfer from the dangling bonds of group III atoms to those of group V atoms.

This occurs by relaxing the surface and pushing the group V atoms outwards and the group III atoms inward. The group V atom's dangling bond is filled, representing surface filled states, and the group III atoms are empty, representing the empty states [57]. However, when measuring GaN under a negative bias, we still observe empty CB states instead of filled states. This happens because empty CB states become filled with carriers at a negative TIBB [47], as we showed in the previous section.

Due to the wide band gap of GaN and because commercial wafers are typically n type, when a negative bias is applied to the clean surface, the accumulation region tunneling current will always form sooner than the tunneling from the valence band states, in contrast to semiconductors with a smaller band gap [see the discussion of the $I(V)$ curve in Sec. III A]. Therefore, in the presence of a clean unpinned surface, when a negative bias is applied, the majority of the tunneling current arises from the Ga atoms and not from the N atoms. Other STM images have been reported for which the authors were able to probe the filled VB states of GaN [10–13,46]. In those experiments the surface Fermi energy was pinned by the defects present, and therefore, a surface accumulation region did not form. Hence, the image reported in Fig. 1(a) is particularly interesting because it shows a defect-free surface. The image was taken at -1.8 V bias voltage, and because of the TIBB the atomic rows that we see in the image are the Ga atom sublattice.

D. Identification of the defect

Typically, the intensity of the feature-related contrast decreases as a function of the depth of the defect below the surface, as we can see from previous work done on single impurities in which the authors were able to distinguish features up to five layers below the surface [33,58,59]. During our measurements all the observed features had similar sizes and shapes, suggesting that all the features are at the same depth and they are related to surface layer defects or impurities. At the surface layer level, the possible sources of such features are adsorbed impurities, dopants, or point defects. Adsorbed impurities depend on a number of factors mainly related to the quality of the vacuum; however, one characteristic of these features is that they tend to increase over time, and it is possible to observe a shift in their position while scanning with the STM. In our measurement we did not observe any variation in the 2-week window of the measurements, and we never observed major shifts in their position. These features cannot be dopants because if they were, we should be able to observe similar features with different contrasts related to different depths below the surface, and this was never observed in the measurements. The last explanation is defects induced during the cleaving of the sample. During an X-STM measurement, it is often possible to encounter missing atoms or even entire stripped-out atomic rows or small areas [60], with depths that go from the single monolayer to a few monolayers.

When looking in more detail into one of the features (e.g., in Fig. 6), we can see that the deepest part (blue cross) lies on top of a corrugation line (red line). This observation, with the knowledge that the corrugation lines represent the Ga atoms, leads us to understand that the feature we are observing is

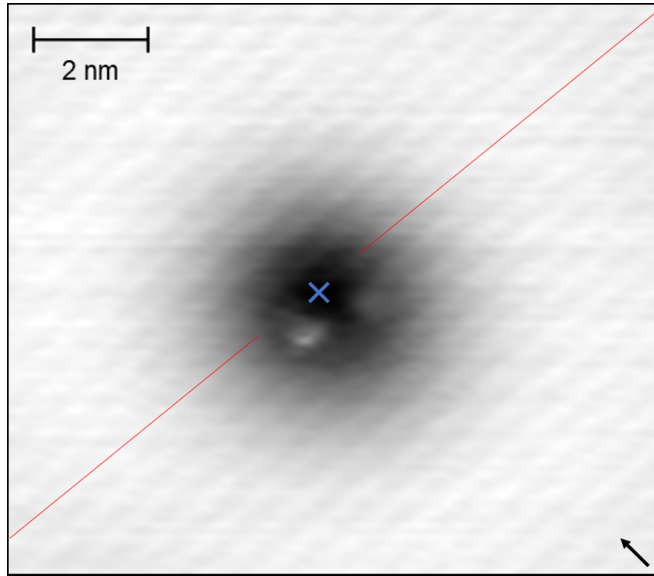


FIG. 6. X-STM image of the Ga vacancy on the GaN m plane, measured at -3.0 V and 50 pA. The black arrow indicates the growth direction $[0001]$, the red line indicates a Ga sublattice corrugation line, the blue cross shows the deepest point in the image, corresponding to the Ga vacancy position. The color scale goes from 0 pm (black) to 90 pm (white). Within the dark contrast region, the core of the feature, there are brighter (higher) parts due to tip imaging.

actually a Ga vacancy. It was already reported that in the case of n -type GaN, the Ga vacancy becomes more energetically favorable [15], although that publication addressed bulk GaN and not the surface.

E. Bistability of the defect

We established that the features we observed during the measurement are surface layer Ga vacancies. In the core of the vacancy (near the blue cross in Fig. 6), there are some bright (higher) areas. We investigated this behavior and noticed that throughout the measurements the appearance of the core was consistent until a major tip change would happen. Following this observation, we deduced it was a tip-related contrast rather than surface related. It is possible that in the presence of a sharp surface state (for example, an adatom or similar point feature), when the tip scans over such a sharp state, a simultaneous imaging of the tip occurs. This creates contrast features that are related not to the sample surface, but rather to the apex of the specific state of the STM tip.

When imaging large areas of the m plane, we observed that the Ga vacancies presented two different structures within the deepest part of the observed feature (see features 1 and 2 in Fig. 7). This result is consistent with the DFT calculations of Hyun and Kim [18], who concluded that around a Ga vacancy in the m -plane surface, the N atom has two possible bistable positional configurations, as described in Fig. 8.

Tip imaging is a known issue that can affect STM measurements. We noticed that in our particular case, it is rather strongly present, and it is capable of imaging many details about the apex of our tip. We believe that is due to a combination of effects; on the one hand, the vacancy

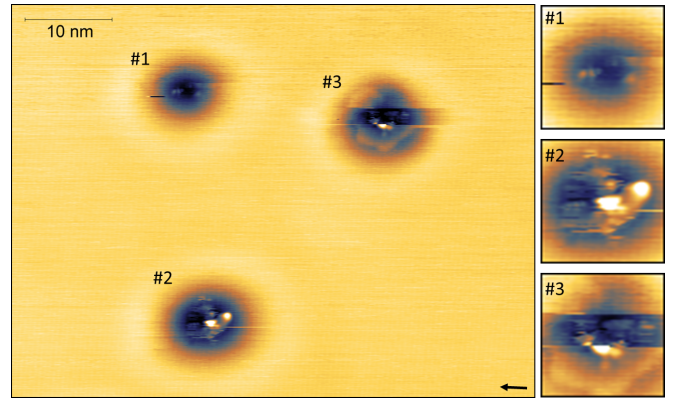


FIG. 7. X-STM image of the GaN m plane taken at -3.2 V and 50 pA. The three features reported in the image as #1, #2 and #3 are Ga vacancies, where in feature 1 the N atom sits in its regular position, in feature 2 it hops towards the next row Ga surface neighboring atom, and in feature 3 the N atom flips between the two possible positions while being measured. On the right we show close-ups of the three features as three images with a size of 7×7 nm².

is a lower-conductivity region that brings the tip in closer proximity to the surface and therefore exposes more of the tip apex. On the other hand, the N atom has two possible “topographical” configurations, one of which can be more efficient in tip imaging due to the highly localized DOS.

If we look at Fig. 7, vacancies 1 and 2 present different core structures, while vacancy 3 switches between the two while being measured. We know from the paper by Hyun and Kim [18] that there are two possible topological configurations for a Ga vacancy in the m plane of GaN. We suggest two different features in X-STM that we expect to correspond to Ga vacancy related features. Another sign that these features correspond to the bistable Ga vacancy is the observed switching behavior shown in Fig. 7 for feature 3. Switching

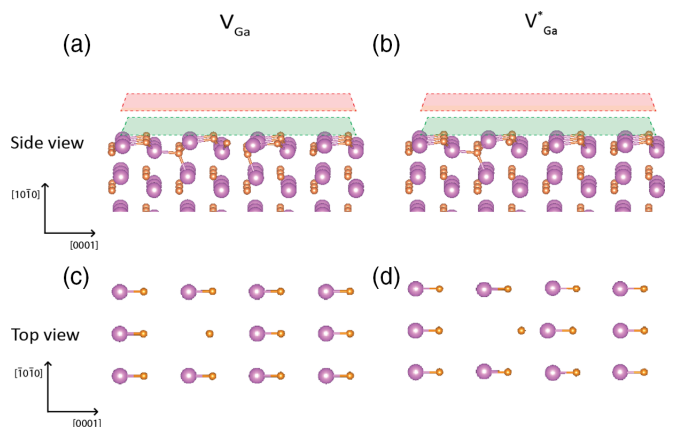


FIG. 8. The supercell used to simulate the m plane of GaN using DFT. In (a) and (b) a side view of the relaxed supercell is shown for the regular V_{Ga} and the Ga vacancy with the displaced N atom V_{Ga}^* , respectively. Also, two planes at 0.75 and 2.75 Å above the surface are shown in green and red, respectively. These planes are indications of the height at which the LDOS will be calculated in Fig. 9. In (c) and (d) a top view of only the topmost GaN layer is shown for the V_{Ga} and V_{Ga}^* configurations, respectively.

of doping atom contrast related to energetic or topographical variations has already been observed in STM measurements (e.g., [61,62]). We therefore propose that the two different features, features 1 and 2, are the two different Ga vacancy configurations. In order to further understand this behavior we performed our own DFT simulations on the defect site to understand how the LDOS is affected by the two topographic configurations.

F. DFT simulations

In order to study the LDOS of this system we use the supercell described in Sec. II, with slight adjustments because of the interest in the Ga vacancy. One Ga atom is now removed in the surface of this supercell in order to simulate this Ga vacancy in the material. An extra charge of three electrons is also introduced in this supercell since that was found to be the lowest energy configuration by Gao *et al.* [15]. The four topmost atomic layers of the supercell are then left to relax until the force on each atom is less than 0.01 eV/\AA . Since a bistability in surface Ga vacancies was found by Hyun and Kim [18], the N atom next to the Ga atom is then moved along the [0001] direction in order to find the second stable atomic configuration. The resulting bond length between the N atom and the nearest Ga atom in the [0001] direction found is 2.048 \AA , which is very similar to the bond length of 1.91 \AA found by Hyun and Kim. This second stable configuration is 316 meV lower in energy than the original relaxation calculation. The LDOSs of the different Ga vacancy configurations are then calculated and compared to the different features found with the X-STM. The relaxed supercell described in Sec. II is presented in Fig. 8. For these calculations the Brillouin zone is sampled using a Monkhorst-Pack grid of $6 \times 6 \times 1$.

We can see the displacement of the N atom towards the neighboring Ga atom when comparing Figs. 8(c) and 8(d). In order to compare the way these two configurations, V_{Ga} and V_{Ga}^* , would appear in our X-STM images, LDOS calculations in different planes in this supercell are performed. In order to calculate the LDOS of a system using the Tersoff-Hamann approximation, we need to decide over which bias we want to integrate the states. Section III explained that even though we perform filled-state imaging, the majority of the tunneling current will come from the lowest conduction band states. The conduction band onset in our DFT calculation is at 1.26 eV . If we use a bias of $+2 \text{ V}$, only the bottom of the conduction band is considered in the LDOS calculations. This should yield the best comparison to the experimental results since the tunneling current is dominated by electrons coming from these states. The LDOS of the system for different heights above the surface of the supercell is given in Fig. 9.

The LDOS of the GaN surface for the two different Ga vacancy configurations is calculated at a distance of 2.75 \AA above the GaN surface. This distance above the surface is chosen since a simulated LDOS is known to correspond well to X-STM measurements for simulated distances of $2\text{--}4 \text{ \AA}$ above the surface [53]. The resulting calculated LDOS at 2.75 \AA above the surface is presented for both the V_{Ga} and V_{Ga}^* configurations in Figs. 9(a) and 9(b). Here we can see that

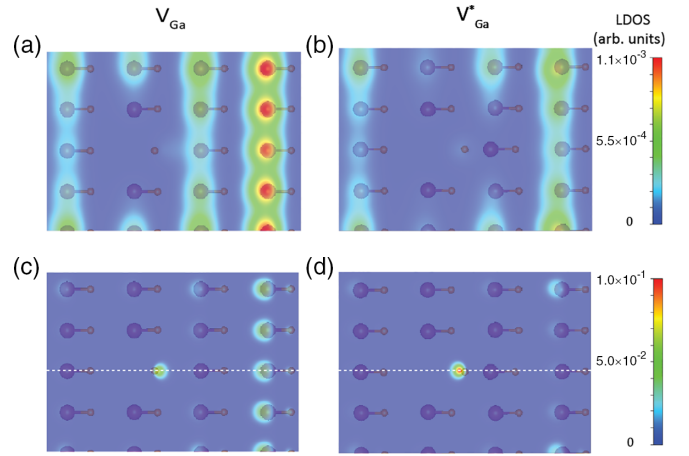


FIG. 9. The LDOS of the $21 \times 16 \text{ \AA}$ GaN supercell simulated for a bias of $+2 \text{ V}$ at different heights above the GaN surface. In (a) and (b) the calculated LDOS is presented at a distance of 2.75 \AA above the GaN surface for the V_{Ga} and V_{Ga}^* configurations, respectively. In (c) and (d) the calculated LDOS is presented at a distance of 0.75 \AA above the GaN surface for the V_{Ga} and V_{Ga}^* configurations, respectively. The dashed white lines in (c) and (d) are the lines along which the line profile is shown in Fig. 10.

both V_{Ga} and V_{Ga}^* result in a decrease in the LDOS around the Ga vacancy. The V_{Ga}^* configuration results in a greater reduction in the LDOS around the Ga vacancy than the V_{Ga} configuration. A lower LDOS would lead to a locally lower tunneling current, and because of this, the tip would move closer to the surface. We have also seen in X-STM measurements that a lower tunneling current around the Ga vacancy is observed, as shown in Fig. 6. We now have both theoretical and experimental indications of the tip moving close to the surface above the Ga vacancy. Because of this, we present a second set of LDOS calculations at 0.75 \AA above the GaN surface in Figs. 9(c) and 9(d). In Figs. 9(c) and 9(d) we observe an isolated peak in the LDOS for both the V_{Ga} and V_{Ga}^* configurations. However, the peak in LDOS is 48% stronger for the V_{Ga}^* configuration. A line profile of the LDOS along the dashed white lines in Figs. 9(c) and 9(d) is presented in Fig. 10 to illustrate the differences between the LDOSs of the two configurations. The V_{Ga} configuration clearly shows a lower peak in LDOS and a stronger corrugation around this peak compared to the V_{Ga}^* configuration.

Both of the features shown in Figs. 9(c) and 9(d) show characteristics that would lead to tip imaging in X-STM. Both consist of an isolated peak in the LDOS where the surrounding LDOS is suppressed. This would lead to the tip moving closer to the surface surrounding the Ga vacancy, and then the strong LDOS on top of the Ga vacancy could image the tip. This matches the behavior we observe for vacancies 1, 2, and 3. We also observe that the image of the tip apex was much stronger for feature 2 than for feature 1. This again matches our calculations since the V_{Ga}^* configuration shows a 48% stronger peak in the LDOS than the V_{Ga} configuration. From this, we conclude that the two different Ga vacancies we label as vacancies 1 and 2 in Fig. 7 are, in fact, the Ga vacancies in the V_{Ga} and V_{Ga}^* configurations, respectively.

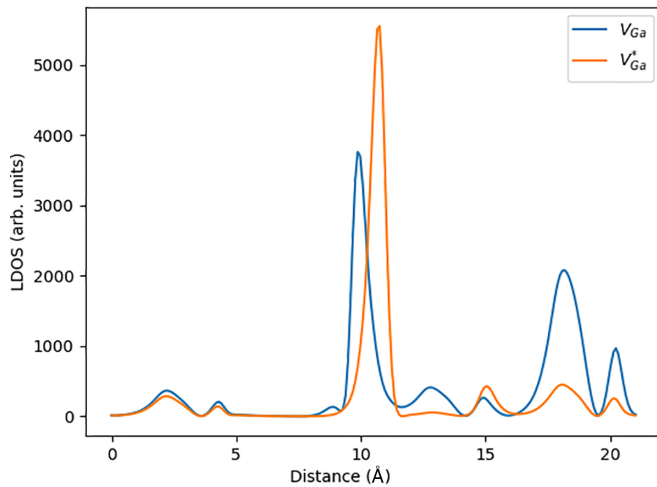


FIG. 10. The LDOS of the GaN supercells along the dashed white lines shown in Fig. 9.

IV. CONCLUSIONS

High-resolution and high-quality cross-sectional scanning tunneling microscopy images of the freestanding GaN non-polar m plane $\{1\bar{1}00\}$ at low temperature were analyzed. When GaN material at negative bias is measured, the observed atomic rows are related to Ga atomic states that are filled due to TIBB accumulation layer formation. This was further supported by simulations of the $I(V)$ curve. When compared to

GaAs, the GaN surface presents a smaller corrugation height of about 5 pm. Due to the smaller corrugation height, the features associated with Ga vacancies show a rather dramatic contrast. We observed the presence of Friedel oscillations around the Ga vacancies, and we were able to experimentally show the dependence of the oscillation radius on the applied bias. The free carriers that screen the local charge are provided by the TIBB accumulation layer, which is dependent on the applied bias. The observed vacancies showed a bistable behavior that was suggested before and further supported by our own DFT simulations. The two possible bistable configurations are due to the neighboring N atom, which can relax to two different positions corresponding to different local bonding configurations. The two configurations give rise to a highly localized LDOS, leading to tip imaging conditions in which it is more severe in one of the two configurations.

ACKNOWLEDGMENTS

We thank the Nederlandse Organisatie voor Wetenschappelijk onderzoek (NWO) for funding this research through the Zwaartekracht project on Integrated Nanophotonics with Project No. 10018478 and for also providing the computational resources needed for this study. NWO granted us access to the Snellius supercomputer in Amsterdam through Project No. EINF-3528, which was used to carry out the DFT calculations. M.E.F. acknowledges that this material is based upon his work supported by the Air Force Office of Scientific Research under Award No. FA9550-22-1-0308.

- [1] K. Iso, H. Yamada, H. Hirasawa, N. Fellows, M. Saito, K. Fujito, S. P. DenBaars, J. S. Speck, and S. Nakamura, *Jpn. J. Appl. Phys.* **46**, L960 (2007).
- [2] D. Zhao, J. Yang, Z. Liu, P. Chen, J. Zhu, D. Jiang, Y. Shi, H. Wang, L. Duan, L. Zhang, and H. Yang, *J. Semicond.* **38**, 051001 (2017).
- [3] J. He, W.-C. Cheng, Q. Wang, K. Cheng, H. Yu, and Y. Chai, *Adv. Electron. Mater.* **7**, 2001045 (2021).
- [4] X. Tang, X. Lu, Z. Cong, Z. Shi, D. Wang, J. Li, X. Ma, and Y. Hao, *Appl. Phys. Lett.* **120**, 033503 (2022).
- [5] M. Rais-Zadeh, V. J. Gokhale, A. Ansari, M. Faucher, D. Theron, Y. Cordier, and L. Buchailot, *J. Microelectromech. Syst.* **23**, 1252 (2014).
- [6] M. Shur, R. Gaska, and A. Bykhovski, *Solid-State Electron.* **43**, 1451 (1999).
- [7] K. T. Upadhyay and M. K. Chattopadhyay, *Mater. Sci. Eng., B* **263**, 114849 (2021).
- [8] O. Katz, D. Misteale, B. Meyler, G. Bahir, and J. Salzman, *IEEE Trans. Electron Devices* **52**, 146 (2005).
- [9] Y.-S. Kang, Q. Fan, B. Xiao, Y. I. Alivov, J. Xie, N. Onojima, S.-J. Cho, Y.-T. Moon, H. Lee, D. Johnstone, H. Morkoç, and Y.-S. Park, *Appl. Phys. Lett.* **88**, 123508 (2006).
- [10] M. Bertelli, P. Löptien, M. Wenderoth, A. Rizzi, R. G. Ulbrich, M. C. Righi, A. Ferretti, L. Martin-Samos, C. M. Bertoni, and A. Cattalani, *Phys. Rev. B* **80**, 115324 (2009).
- [11] C. D. Lee, R. M. Feenstra, J. E. Northrup, L. Lymperakis, and J. Neugebauer, *MRS Proc.* **743**, 41 (2011).
- [12] C. D. Lee, R. M. Feenstra, J. E. Northrup, L. Lymperakis, and J. Neugebauer, *Appl. Phys. Lett.* **82**, 1793 (2003).
- [13] L. Ivanova, S. Borisova, H. Eisele, M. Dähne, A. Laubsch, and P. Ebert, *Appl. Phys. Lett.* **93**, 192110 (2008).
- [14] S. Limpijumngong and C. G. Van de Walle, *Phys. Rev. B* **69**, 035207 (2004).
- [15] Y. Gao, D. Sun, X. Jiang, and J. Zhao, *J. Appl. Phys.* **125**, 215705 (2019).
- [16] J. L. Lyons, A. Janotti, and C. G. Van de Walle, *Phys. Rev. B* **89**, 035204 (2014).
- [17] C. E. Dreyer, A. Alkauskas, J. L. Lyons, J. S. Speck, and C. G. Van de Walle, *Appl. Phys. Lett.* **108**, 141101 (2016).
- [18] J.-M. Hyun and H. Kim, *J. Korean Phys. Soc.* **68**, 420 (2016).
- [19] M. Monavarian, A. Rashidi, and D. Feezell, *Phys. Status Solidi A* **216**, 1800628 (2019).
- [20] C. B. Lim, A. Ajay, and E. Monroy, *Appl. Phys. Lett.* **111**, 022101 (2017).
- [21] A. Rashidi, M. Monavarian, A. Aragon, A. Rishinaramangalam, and D. Feezell, *IEEE Electron Device Lett.* **39**, 520 (2018).
- [22] C. B. Lim, A. Ajay, C. Bougerol, J. Lähnemann, F. Donatini, J. Schörmann, E. Bellet-Amalric, D. A. Browne, M. Jiménez-Rodríguez, and E. Monroy, *Nanotechnology* **27**, 145201 (2016).
- [23] C. Edmunds, J. Shao, M. Shirazi-HD, M. J. Manfra, and O. Malis, *Appl. Phys. Lett.* **105**, 021109 (2014).
- [24] L. Wang, T.-T. Lin, M.-X. Chen, K. Wang, and H. Hirayama, *Appl. Phys. Express* **14**, 112003 (2021).
- [25] K. A. Bertness, A. Roshko, L. M. Mansfield, T. E. Harvey, and N. A. Sanford, *J. Cryst. Growth* **300**, 94 (2007).
- [26] S. D. Hersee, X. Sun, and X. Wang, *Nano Lett.* **6**, 1808 (2006).
- [27] S. Nakamura, *Semicond. Sci. Technol.* **14**, R27 (1999).

- [28] S. Cuesta, L. Denaix, F. Castioni, L. S. Dang, and E. Monroy, *Semicond. Sci. Technol.* **37**, 075013 (2022).
- [29] R. S. R. Gajjela, E. M. Sala, J. Heffernan, and P. M. Koenraad, *ACS Appl. Nano Mater.* **5**, 8070 (2022).
- [30] R. S. R. Gajjela, N. R. S. van Venrooij, A. R. da Cruz, J. Skiba-Szymanska, R. M. Stevenson, A. J. Shields, C. E. Pryor, and P. M. Koenraad, *Nanotechnology* **33**, 305705 (2022).
- [31] R. S. R. Gajjela and P. M. Koenraad, *Nanomaterials* **11**, 85 (2021).
- [32] R. S. R. Gajjela, A. L. Hendriks, J. O. Douglas, E. M. Sala, P. Steindl, P. Klenovský, P. A. J. Bagot, M. P. Moody, D. Bimberg, and P. M. Koenraad, *Light: Sci. Appl.* **10**, 125 (2021).
- [33] C. M. Krammel, A. R. da Cruz, M. E. Flatté, M. Roy, P. A. Maksym, L. Y. Zhang, K. Wang, Y. Y. Li, S. M. Wang, and P. M. Koenraad, *Phys. Rev. B* **101**, 024113 (2020).
- [34] C. M. Krammel, L. Nattermann, E. Sterzer, K. Volz, and P. M. Koenraad, *J. Appl. Phys.* **123**, 161589 (2018).
- [35] R. C. Plantenga, V. R. Kortan, T. Kaizu, Y. Harada, T. Kita, M. E. Flatté, and P. M. Koenraad, *Phys. Rev. B* **96**, 155210 (2017).
- [36] H. P. Ebert, *Mater. Today* **6**, 36 (2003).
- [37] J. C. Zolper, M. Hagerott Crawford, A. J. Howard, J. Ramer, and S. D. Hersee, *Appl. Phys. Lett.* **68**, 200 (1996).
- [38] D. M. Hofmann, D. Kovalev, G. Steude, B. K. Meyer, A. Hoffmann, L. Eckey, R. Heitz, T. Detchprom, H. Amano, and I. Akasaki, *Phys. Rev. B* **52**, 16702 (1995).
- [39] G. Yi and B. W. Wessels, *Appl. Phys. Lett.* **69**, 3028 (1996).
- [40] J. Pankove, S. Bloom, and G. Harbeke, *RCA Rev.* **36**, 163 (1975), <https://worldradiohistory.com/ARCHIVE-RCA/RCA-Review/RCA-Review-1975-Mar.pdf>.
- [41] P. E. Blöchl, *Phys. Rev. B* **50**, 17953 (1994).
- [42] G. Kresse and J. Furthmüller, *Comput. Mater. Sci.* **6**, 15 (1996).
- [43] G. Kresse and J. Furthmüller, *Phys. Rev. B* **54**, 11169 (1996).
- [44] J. P. Perdew, K. Burke, and M. Ernzerhof, *Phys. Rev. Lett.* **77**, 3865 (1996).
- [45] H. Schulz and K. Thiemann, *Solid State Commun.* **23**, 815 (1977).
- [46] L. Freter, Y. Wang, M. Schnedler, J.-F. Carlin, R. Butté, N. Grandjean, H. Eisele, R. E. Dunin-Borkowski, and P. Ebert, *J. Appl. Phys.* **128**, 185701 (2020).
- [47] R. M. Feenstra, Y. Dong, M. P. Semtsiv, and W. T. Masselink, *Nanotechnology* **18**, 044015 (2007).
- [48] P. Ebert, L. Ivanova, and H. Eisele, *Phys. Rev. B* **80**, 085316 (2009).
- [49] M. Schnedler, V. Portz, H. Eisele, R. E. Dunin-Borkowski, and P. Ebert, *Phys. Rev. B* **91**, 205309 (2015).
- [50] L. Lymperakis, P. H. Weidlich, H. Eisele, M. Schnedler, J.-P. Nys, B. Grandidier, D. Stiévenard, R. E. Dunin-Borkowski, J. Neugebauer, and P. Ebert, *Appl. Phys. Lett.* **103**, 152101 (2013).
- [51] N. Ishida, K. Sueoka, and R. M. Feenstra, *Phys. Rev. B* **80**, 075320 (2009).
- [52] R. M. Feenstra, S. Gaan, G. Meyer, and K. H. Rieder, *Phys. Rev. B* **71**, 125316 (2005).
- [53] D. Tjeertes, A. Vela, T. J. F. Verstijnen, E. G. Banfi, P. J. van Veldhoven, M. G. Menezes, R. B. Capaz, B. Koiller, and P. M. Koenraad, *Phys. Rev. B* **104**, 125433 (2021).
- [54] J. Friedel, *London, Edinburgh, Dublin Philos. Mag. J. Sci.* **43**, 153 (1952).
- [55] M. C. M. M. van der Wielen, A. J. A. van Roij, and H. van Kempen, *Phys. Rev. Lett.* **76**, 1075 (1996).
- [56] G. J. de Raad, D. M. Bruls, P. M. Koenraad, and J. H. Wolter, *Phys. Rev. B* **66**, 195306 (2002).
- [57] R. M. Feenstra, J. A. Stroscio, J. Tersoff, and A. P. Fein, *Phys. Rev. Lett.* **58**, 1192 (1987).
- [58] J. M. Ulloa, P. M. Koenraad, and M. Hopkinson, *Appl. Phys. Lett.* **93**, 083103 (2008).
- [59] A. P. Wijnheijmer, J. K. Garleff, K. Teichmann, M. Wenderoth, S. Loth, R. G. Ulbrich, P. A. Maksym, M. Roy, and P. M. Koenraad, *Phys. Rev. Lett.* **102**, 166101 (2009).
- [60] C. Çelebi, O. Arı, and R. T. Senger, *Phys. Rev. B* **87**, 085308 (2013).
- [61] E. P. Smakman, P. L. J. Helgers, J. Verheyen, P. M. Koenraad, and R. Möller, *Phys. Rev. B* **90**, 041410(R) (2014).
- [62] D. Tjeertes, T. J. F. Verstijnen, A. Gonzalo, J. M. Ulloa, M. S. Sharma, M. Felici, A. Polimeni, F. Biccari, M. Gurioli, G. Pettinari, C. Sahin, M. E. Flatté, and P. M. Koenraad, *Phys. Rev. B* **102**, 125304 (2020).